Applied Clay Science 242 (2023) 107018

Contents lists available at ScienceDirect

Applied Clay Science

journal homepage: www.elsevier.com/locate/clay

Research paper

A non-isothermal reactive transport model of the long-term geochemical evolution at the disposal cell scale in a HLW repository in granite

Luis Montenegro [a], Javier Samper [a,*], Alba Mon [a], Laurent De Windt [b], Aurora-Core Samper [a], Enrique García [c]

[a] Interdisciplinar Center of Chemistry and Biology (CICA), Civil Engineering, Campus de Elviña, University of A Coruña, 15071 A Coruña, Spain
[b] MINES Paris, PSL University, Centre for Geosciences and Geoengineering, Fontainebleau, France
[c] ENRESA, Madrid, Spain

ARTICLE INFO

Keywords:
THC model
Bentonite
Corrosion products
Reactive transport
Canister corrosion
International Simple Glass

ABSTRACT

The assessment of the long-term performance of the engineered barrier systems of high-level radioactive waste (HLW) repositories requires the use of reactive transport models. Here a non-isothermal reactive transport model of the long-term geochemical evolution of a HLW disposal cell in a granitic host rock is presented. The model includes the vitrified waste (40 cm in diameter), the carbon-steel canister (5 cm thick), the saturated FEBEX bentonite buffer (75 cm thick) and the reference granitic rock. The model accounts for the thermal transient stage and assumes generalized steel corrosion under anaerobic conditions with a corrosion rate equal to 1.41 m/y. Canister failure is assumed to occur when the remaining canister thickness is equal to 3.5 cm at $t = 25{,}000$ years. Canister corrosion caused an increase in pH. The computed pH in the canister just before canister failure ($t = 25{,}000$ years) was equal to 9.25 and ranged from 7.82 to 9.25 in the bentonite. Magnetite, the main corrosion product, precipitated in the bentonite and especially in the canister. The thickness of magnetite precipitation band in the bentonite was ≈ 1 cm. Siderite precipitated at both sides of the canister/bentonite interface. The precipitation front penetrated >1 cm into the bentonite. Nuclear glass started dissolving after canister failure ($t > 25{,}000$ years). The concentration of dissolved silica increased in the inner part of the glass until $t = 30{,}000$ years and decreased in the outer part of the glass due to the out diffusion of dissolved silica into the canister and the bentonite. This diffusive flux caused the precipitation of greenalite at the glass/canister and canister/bentonite interfaces. The pH at the end of the simulation ($t = 50{,}000$ years) ranged from 7.93 to 7.89 in the glass, from 7.89 to 8.66 in the canister and from 7.87 to 8.6 in the bentonite. Magnetite precipitated in the canister while there was carbon steel to corrode. Once the canister was fully corroded, magnetite redissolved near the glass/canister interface. Greenalite precipitated in the canister and the bentonite, especially at the glass/canister interface and siderite precipitated at the canister/bentonite interface. The simulation results should be useful for the performance assessment of engineered barriers of radioactive waste repositories in granitic host rocks.

1. Introduction

The disposal of high-level radioactive waste (HLW) in a deep geological repository (DGR) is based on a multi-barrier concept, which includes the host rock and the engineered barrier system (EBS). The EBS in a HLW disposal cell in a granitic formation includes the vitrified waste, the canister and the compacted bentonite. Assessing the performance of the EBS requires the use of reactive transport models to simulate the reactions at the interfaces of these reactive materials (De Windt and Spycher, 2019; Claret et al., 2022). Bildstein et al. (2019) showed that most of the physical and chemical reactivity in a DGR is concentrated at the interfaces of different materials (vitrified waste, steel/iron, bentonite, cement/concrete, and the granite or clay host rock). According to these authors, it is necessary to predict: (1) The alteration extent and the distance at which the perturbations will progress into the barriers; and (2) The material properties evolution in these barriers resulting from their alteration and to assess the impact on the overall performance and safety of the repository.

Deissmann et al. (2021) presented a compilation of the existing knowledge on relevant processes occurring at the interfaces between the

* Corresponding author.
E-mail address: j.samper@udc.es (J. Samper).

https://doi.org/10.1016/j.clay.2023.107018
Received 5 February 2023; Received in revised form 12 May 2023; Accepted 28 May 2023
Available online 9 June 2023

different materials relevant for the chemical evolution of intermediate-level radioactive waste (ILW) and HLW disposal cells in several European repository concepts. The geochemical interactions at the steel/iron-bentonite interface have been studied in laboratory tests and in situ experiments in underground research laboratories and have been quantified with reactive transport models. Detailed compilations of steel/iron-clay interactions have been reported by Marty et al. (2010), Savage et al. (2010), Savage (2012), Bildstein and Claret (2015), Samper et al. (2016), Mon et al. (2017), Claret et al. (2018), Bildstein et al. (2019), Deissmann et al. (2021) and Mon et al. (2023).

Bildstein et al. (2019) presented a comprehensive review of the reactive transport models of the iron-clay interface at different scales. They concluded that: (1) Magnetite is the main corrosion product. Other corrosion products include Fe-phyllosilicates such as greenalite, berthierine and cronstedtite and Fe-carbonates such as siderite; (2) Model predictions are very sensitive to the corrosion rate; and (3) The thickness of the clay alteration is predicted to be a few cm (up to 20 cm). Deissmann et al. (2021) presented an in-depth compilation of the main assumptions, corrosion rates, main corrosion products, secondary minerals, maximum perturbation extent and other relevant results of recent reactive transport models of the steel/iron-bentonite interface at the disposal scale.

Reactive transport models of the chemical evolution of the glass/steel interface at the scale and time (100,000 years) of a HLW disposal cell are scarce (Bildstein et al., 2007, 2012, 2019). De Windt et al. (2006) assessed the long-term (100,000 years) evolution of nuclear glass in a HLW repository in clay considering silica diffusion, sorption and precipitation processes. This performance assessment (PA) study focused on the geochemical interactions between glass, corroded steel, and the host rock by using a congruent kinetic dissolution rate law for R7T7 glass. The kinetic rate law includes a first-order term which depends on the concentration of silica and a long-term constant residual term. Modeling the dissolution of the vitrified waste is a critical aspect for predicting the chemical evolution in a HLW disposal cell in granite. The GRAAL model (Frugier et al., 2008, 2018; Debure et al., 2013, 2019) couples the primary glass alteration rate, controlled by a protective layer's thickness, and the dissolution rate of the protective layer in interaction with the environment.

Here a non-isothermal multicomponent reactive transport model of the long-term geochemical evolution in a HLW disposal cell in granite is presented, which goes beyond the models reported so far by considering besides steel corrosion and the interactions of corrosion products and bentonite, the glass dissolution and the interactions of glass, steel, and corrosion products. The paper starts with the description of the HLW disposal cell in granite, the conceptual and numerical models, and the computer code. Then, model predictions are presented for the base run for Periods II ($0 < t < 25{,}000$ years) and III ($25{,}000 < t < 50{,}000$ years). Afterwards, the sensitivity analysis is presented. The paper ends with the main conclusions.

2. Description of the HLW disposal cell in granite

The HLW disposal cell concept in granitic host rock includes: (1) The vitrified waste (40 cm in diameter) which is explicitly considered in the reactive transport model and is coupled with the rest of the engineered barrier components; (2) The canister which is a carbon-steel canister (5 cm thick); (3) The bentonite buffer (75 cm thick) which is composed of water-saturated FEBEX bentonite with a dry density of 1600 kg/m^3; and (4) The Spanish Reference Granitic (SRG) host rock (25 m) (Fig. 1). This HLW disposal cell concept in granite is not specific of any country, but aims at representing several national concepts. This concept is based on the Spanish spent fuel reference concept in granite, known as ENRESA 2000 (ENRESA, 2001). The main differences between these two concepts are the type of waste (vitrified waste vs. spent fuel) and the dimensions of the carbon-steel canister (45 cm in diameter for vitrified waste and 90 cm for spent fuel). The materials and dimensions of the nuclear waste form, the canister, the engineered barrier and the host rock selected for the HLW disposal cell in granite were taken from Samper et al. (2022).

In ENRESA (2001) the carbon steel canisters wee placed on horizontal disposal drifts with a separation of 2 m from one another. Canisters were surrounded by high-density blocks of bentonite which were initially unsaturated with a gravimetric water content of 14%. The disposal drifts of 500 m in length and 2.4 m in diameter were located at a depth of 500 m in the granitic host formation and separated 35 m to prevent exceeding a temperature of 100 °C in the bentonite. The access was accomplished by “main drifts” which run perpendicular to the disposal drifts. The main drifts met at a central area, which includes the required underground infrastructure (Fig. 1). The granitic formation was selected to have a low fracture density, tectonic stability, low seismicity and appropriate geochemical conditions.

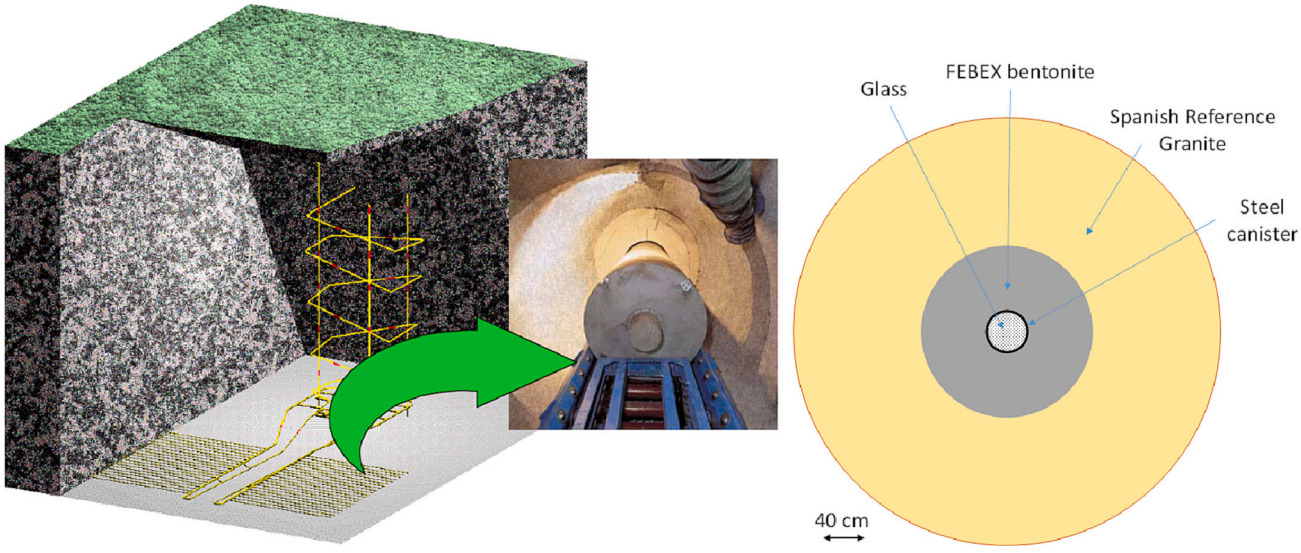

Fig. 1. Underground installations of a radioactive waste repository in granite according to the Spanish Reference Concept for spent fuel (ENRESA, 2001). Layout of the representative HLW disposal cell concept in a granitic host rock selected in the ACED Work Package of the EURAD Project (Samper et al., 2022) which includes the vitrified waste (40 cm diameter), the steel canister (5 cm thick), the FEBEX bentonite buffer (75 cm thickness) and the Spanish Reference Granite.

3. Conceptual THC model

The non-isothermal multicomponent reactive transport model of the HLW disposal cell in granite involves the bentonite/granitic host rock, carbon-steel/bentonite and vitrified waste/carbon-steel canister interfaces. The model considers three successive periods. Period I covers the oxic transient stage. Period II starts when the bentonite is fully saturated and anoxic conditions are prevailing. Canister corrosion, the interactions of corrosion products and the bentonite and the interactions of bentonite and granite are considered in this period. Finally, Period III starts after canister failure and considers glass alteration and the interactions of glass with corrosion products and uncorroded iron. Here a model for Periods II and III is reported.

3.1. Hydrodynamic processes

The bentonite is expected to become fully saturated in <50 years (Zheng and Samper, 2008). The reactive transport model assumes that the bentonite is initially water saturated. The hydraulic conductivity of the bentonite is extremely low. Therefore, advection is negligible and solute diffusion is the main solute transport mechanism in the bentonite (Samper et al., 2006). All the water is assumed to be accessible to solutes. Solute transport processes in the granite include molecular diffusion and advection which is assumed to be parallel to the axis of the gallery.

Steel canister corrosion may induce two-phase water flow due to the water consumption by corrosion and hydrogen gas pressure build-up (Xu et al., 2008). As pointed out by Ortiz et al. (2002), it is assumed in the model that H_2(g) migrates through cyclic opening and closure of discrete preferential pathways. Therefore, partial desaturation of the bentonite due to the formation of a gas phase is disregarded in the HLW disposal cell in granite. The model considers the diffusion of dissolved hydrogen, H_2(aq).

3.2. Thermal processes

The reactive transport model considers the thermal transient stage and the cooling of the vitrified waste. The time evolution of the temperatures was calculated by assuming a storage time, which ranges from 100 to 170 years, during which the fuel elements are kept releasing heat and radioactivity to acceptable levels. These calculations were based on the requirement that the temperature in the bentonite does not exceed 100 °C and correspond to (Neeft et al., 2020): 1) Vitrified waste (0.42 m of diameter), 2) Stainless steel (5 mm thick), 3) Air gap (13 mm thick), 4) Carbon-steel canister (7.5 cm), 5) Bentonite (75 cm); and 6) Granitic rock (100 m long). The temperature at the interface carbon-steel/bentonite reaches the host rock ambient temperature of 32 °C at t = 3000 years (Fig. 1 in Supplementary Material, SM).

3.3. Chemical processes

The conceptual geochemical model includes: 1) Carbon-steel canister corrosion, 2) Vitrified waste dissolution, 3) Aqueous complexation; 4) Acid/base; 5) Redox; 6) Mineral dissolution/precipitation; 7) Cation exchange of Ca^{2+}, Mg^{2+}, Fe^{2+}, Na^+ and K^+; and 8) Surface complexation of H^+ and Fe^{2+} on strong sites, S^sOH, weak #1 sites, $S^{w1}OH$ and weak #2 sites, $S^{w2}OH$. Cation exchange and surface complexation reactions occur only in the bentonite.

The geochemical system is defined in terms of H_2O, H^+, O_2(aq), Ca^{2+}, Mg^{2+}, Na^+, K^+, Fe^{2+}, Al^{3+}, Cl^-, SO_4^{2-}, HCO_3^-, H_4SiO_4(aq), $B(OH)_4^-$, 39 secondary aqueous species, 11 minerals, 5 exchanged cations and 13 surface complexes (Table 1 and Table 2 in SM). The Gaines-Thomas convention is used for cation exchange reactions (Appelo and Postma, 1993). Surface complexation reactions in the bentonite were modelled with the non-electrostatic triple-site sorption model of Bradbury and Baeyens (1997, 2005).

All the reactions are assumed at chemical equilibrium, except for carbon-steel corrosion and smectite dissolution which are kinetically controlled. The kinetic rate is given by:

$$r_m = k_m e^{\frac{-Ea}{RT}} \left| \left(\Omega_m^{\theta} - 1\right)^{\eta} \right| \quad (1)$$

where r_m is the dissolution/precipitation rate (mol/m^2/s), k_m is the kinetic rate constant (mol/m^2/s) at 25 °C, Ea is the activation energy, R is the gas constant (J/K·mol), T is the absolute temperature (K), Ω_m is the saturation index which is equal to the ratio of the ion activity product to the equilibrium constant (dimensionless), and θ and η are kinetic parameters.

3.3.1. Carbon steel corrosion

The available oxygen in the HLW disposal cell in granite is consumed soon after its closure, and anaerobic conditions are expected to prevail in the long term. The canister is treated as a porous material made of metallic iron, Fe(s). Under anaerobic conditions, H_2O is the oxidizing agent of Fe(s) (Lu et al., 2011; Samper et al., 2016; and Mon et al., 2017) according to:

$$Fe(s) + 2H^+ + 0.5O_2(aq) \Leftrightarrow Fe^{2+} + H_2O \quad (2)$$

Carbon-steel corrosion is kinetically controlled. The base run assumes a constant corrosion rate. The corrosion rate is equal to 1.41 μm/year (Samper et al., 2016; Mon et al., 2017). Period II is assumed to last 25,000 years. The density of the canister is equal to 7600 kg/m^3.

3.3.2. Vitrified waste dissolution

A simplified version of the composition of the vitrified waste was adopted by using the ISG (International Simple Glass) (see Samper et al., 2022). The ISG has a chemical composition like the French reference glass, SON-68. These glasses differ only on minor components such as Ba, Ln or Mo (Debure et al., 2012; Gin et al., 2015). The main component of the chemical composition (in weight %) of the ISG is SiO_2 with a 56.2%, followed by B_2O_3 with a 17.3%, Na_2O with a 12.2%, Al_2O_3 with a 6%, CaO with a 5% and ZrO_2 with a 3.3%. The very low Zr content of the ISG was, however, skipped for the sake of improving the convergence of the iterative calculations. This is a simplified ISG composition in which radioactive elements have been neglected. The calculated molecular weight of the ISG is 19.25 g/mol and its molar volume is 7.70 cm^3/mol.

The model presented here relies on the dissolution rate of the R7T7 glass reported by De Windt et al. (2006). The dissolution of the glass is controlled by two temperature-dependant kinetic terms according to the conceptual model of Gin et al. (2013). The kinetic dissolution rate includes an initial dissolution rate, r_0, and a long-term residual rate r_r. By assuming a congruent dissolution of the vitrified waste, these two kinetic terms can be modelled by: (1) A first-order initial dissolution rate (Jollivet et al., 2000, 2012) which is chemistry-dependant (pH and dissolved silica concentration); and (2) A long-term residual dissolution rate which is chemistry-independent (Gin and Frugier, 2002; Gin et al., 2015). The kinetic rate law becomes:

$$\frac{d[glass]}{dt} = -k_{0,pH}\,(H^+)^{-0.4}\,\sigma\left(1 - \frac{C_{Si}}{C_{Si}^*}\right) - k_r\,\sigma \quad (3)$$

where $k_{0,pH}$ is the initial kinetic constant (mol/m^2·s), $(H^+)^{-0.4}$ is a proton activity term, σ is the glass reactive surface, C_{Si} is the concentration of dissolved silica, C_{Si}^* is a threshold silica concentration which ensures that glass dissolution stops when $C_{Si} > C_{Si}^*$ and k_r is the residual kinetic rate constant (mol/m^2·s).

The kinetic parameters of Eq. (3) used by De Windt et al. (2006) were derived from leaching experiments performed at 90 °C in pure water and in the pH range 6–10. The conditions of the present model in granite correspond to lower temperatures and more complex aqueous solution. Therefore, the first-order initial dissolution rate has been updated from the experiments of Jollivet et al. (2012) performed at 30 °C and 50 °C

with synthetic claystone porewater. The long-term residual dissolution rate was estimated from the experiments of Fleury et al. (2014) done in pure water at 30 °C and 50 °C. It is important to point out that the model assumes that only the congruent glass dissolution can take place in the glass subdomain. No other mineral phases are allowed to dissolve or precipitate in the portion of the model domain occupied by the glass.

According to De Windt et al. (2006), the most critical parameter in the R7T7 dissolution rate is the threshold silica concentration at saturation C^*_{Si}. The impact of the uncertainty in the value of threshold silica concentration in model predictions has been evaluated with sensitivity runs. The dissolution rate increases with pH and decreases when the threshold silica concentration increases (Fig. 1 in SM).

3.3.3. Smectite dissolution

Smectite dissolution is simulated by assuming the chemical formulation of the FEBEX bentonite proposed by Fernández et al. (2009) and by using the kinetic rate law of Eq. (1). The kinetic rate constant, k_m, at 25 °C is $1.58{\cdot}10^{-13}$ mol/m^2·s (Cama et al., 2000; Bildstein et al., 2006; Chaparro et al., 2021). The activation energy, *Ea*, is 60 KJ/mol (Chaparro et al., 2021). Kinetic parameters θ and η are equal to 1. The smectite specific surface area, σ, is 10 times smaller than the value proposed by Fernández et al. (2009) (250 dm^2/L). This value leads to dissolution rates similar to those of Chaparro et al. (2021).

4. Numerical model

4.1. Finite element grid and time periods

The model was performed with a non-uniform 1-D axisymmetric finite element mesh with 152 nodes (see more details and Fig. 2 in SM). Model predictions were performed for Periods II (canister corrosion) and III (glass dissolution). Period II lasts for 25,000 years before canister failure. Period III starts at $t = 25{,}000$ years and considers glass dissolution. The final simulation time is $t = 50{,}000$ years.

4.2. Flow and transport parameters

The model assumes that the glass fracture network can be represented as an equivalent porous medium. Glass porosity was taken equal to 0.3 and an effective diffusion coefficient $D_e = 10^{-10}$ m^2/s (De Windt et al., 2006). The flow and transport parameters are listed in Table 1. Water flow through the granite is simulated with a constant water flux of 0.1 L/year parallel to the axis of the gallery. The hydraulic conductivity of the granite is $8.72{\cdot}10^{-12}$ m/s. The effects of the excavation damaged zone (EDZ) and a larger hydraulic conductivity of the host rock are evaluated in a sensitivity run. The hydraulic conductivity of the EDZ is $8.72{\cdot}10^{-11}$ m/s (Samper et al., 2022).

Table 1
Thermal and hydrodynamic parameters of the glass, canister, bentonite, excavation damaged zone (EDZ) and granite (ENRESA, 2006; Zheng and Samper, 2008; Zheng et al., 2011; Samper et al., 2016, 2018).

Parameter	Glass	Canister	Bentonite	EDZ	Granite
Porosity	0.3	0.3	0.407	0.005	0.005
Efective diffusion coeficient (m^2/s)	10^{-10}	$2.72{\cdot}10^{-11}$	$4.07{\cdot}10^{-11}$	$5.02{\cdot}10^{-14}$	$5.02{\cdot}10^{-14}$
Solid density (kg/m^3)	2513	2513	2700	2700	2700
Thermal conductivity of the solid (W/m °C)	1	50	1.15	1.5	1.5

4.3. Chemical parameters

The initial chemical compositions of the bentonite, EDZ and granite porewaters were taken from Samper et al. (2016) (Table 3 in SM). As an educated guess, the initial porewater compositions of the glass and canister porewaters were taken equal to that of the bentonite porewater. The initial accessory mineral volume fractions in the bentonite include calcite (1%) and smectite (57%). The initial mineral volume fraction of calcite in the granite is 5%. The initial volume fraction of Fe(s) in the canister is 0.99 and the initial volume fraction of ISG in the glass is equal to 0.7.

Kinetic and parameters of the ISG were derived from De Windt et al. (2006) (see Table 2). The cation exchange capacity (CEC) of the bentonite is 102 meq/100 g (Fernández et al., 2004). Cation selectivity coefficients for exchanged Ca^{2+}, Mg^{2+}, K^+ and Fe^+ were taken from Samper et al. (2008) and Tournassat et al. (2008) (Table 2 in SM). Surface complexation reactions in the bentonite are modelled with the triple sorption site model of Bradbury and Baeyens (1997, 2005). The total concentration of sorption sites is 0.322 mol/L.

4.4. Computer code

Model simulations were performed with the finite element reactive transport code CORE^{2D} V5 (Molinero et al., 2004; Zhang et al., 2008; Samper et al., 2009; Fernández, 2017; Águila et al., 2020). CORE^{2D} V5 relies on several thermodynamic databases. ThermoChimie v10.a (Giffaut et al., 2014) was used for the model presented here. CORE^{2D} V5 is based on the sequential iteration approach, considers the changes in porosity due to mineral dissolution/precipitation reactions and their feedback effect on the flow and transport parameters (Samper et al., 2009; Águila et al., 2020). The code has been benchmarked against other reactive transport codes (Poonoosamy et al., 2018; Águila et al., 2021).

5. Model results for Period II

Period II started when the bentonite was fully saturated and anoxic conditions wee prevailing. Canister corrosion, the interactions of corrosion products and the bentonite, and the interactions of bentonite and granite were considered in this period. Period II was assumed to last 25,000 years which coincides with canister failure when which the remaining thickness of the canister is 1.5 cm.

Canister corrosion caused an increase in pH (Fig. 2) in the canister and the bentonite near the bentonite interface. The computed pH at the end of Period II (25,000 years) was equal to 9.25 in the canister and ranges from 9.25 to 7.82 in the bentonite. The concentration of dissolved Fe increased in the first 1000 years and later decreased (Fig. 2). The time evolution of the computed pH and the concentration of dissolved Fe was controlled by: 1) The dissolution/precipitation of Fe minerals in the canister and in the bentonite near the canister interface, 2) Fe exchange, and 3) Fe and proton surface complexation reactions.

Magnetite precipitation took place mostly in the canister and proceeded as long as the canister was corroding (Fig. 3). The thickness of

Table 2
Initial and residual kinetic constants, $k_{0,pH}$ and k_r, threshold silica concentration, C^*_{Si}, specific surface, σ, and effective diffusion coefficient of the ISG (De Windt et al., 2006).

Parameter	Value
$k_{0,pH}$ [mol/m^2/s]	$1.8{\cdot}10^{-11}$
k_r [mol/m^2/s]	$6{\cdot}10^{-11}$
C^*_{Si} [mol/L]	10^{-3}
σ [dm^2/L]	29.2
D_e [m^2/s] for $0 < t < 25{,}000$ years	10^{-20}
D_e [m^2/s] for $t > 25{,}000$ years	10^{-10}

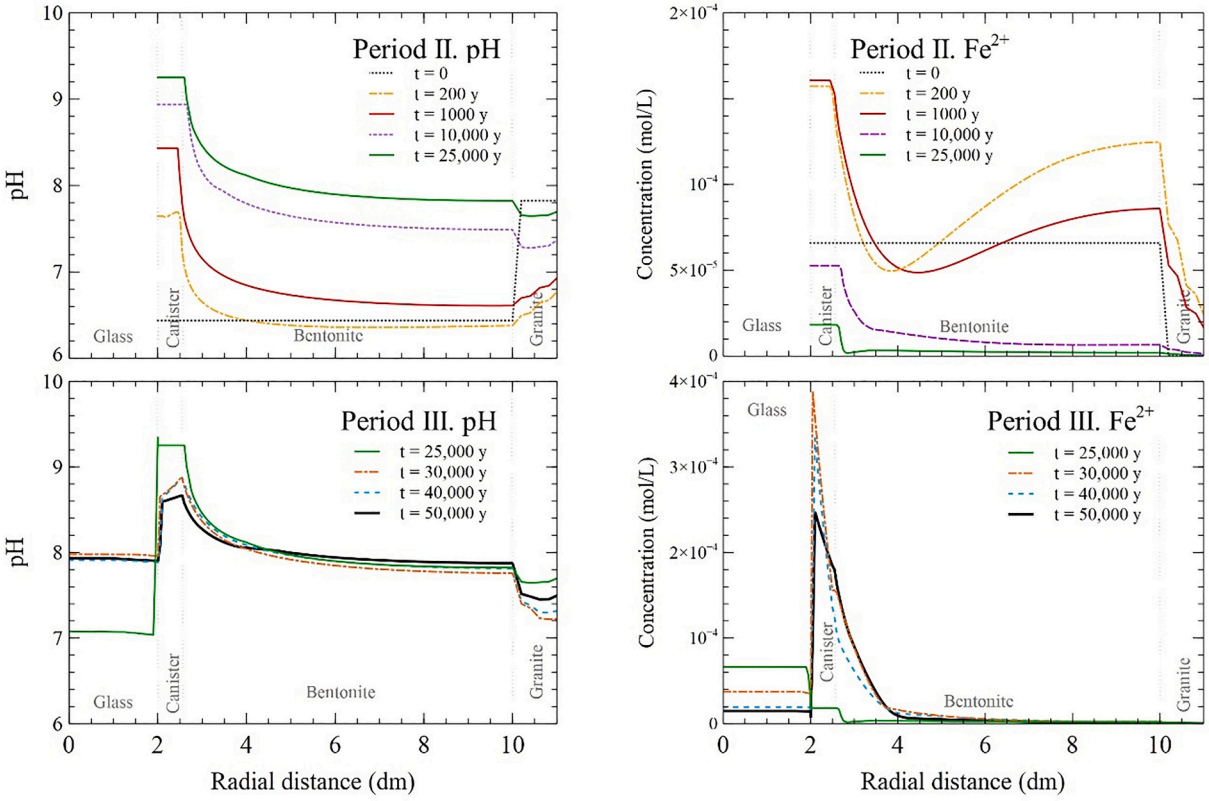

Fig. 2. Spatial distribution of the computed pH (left) and dissolved Fe concentration (right) at selected times of Periods II (top) and III (bottom).

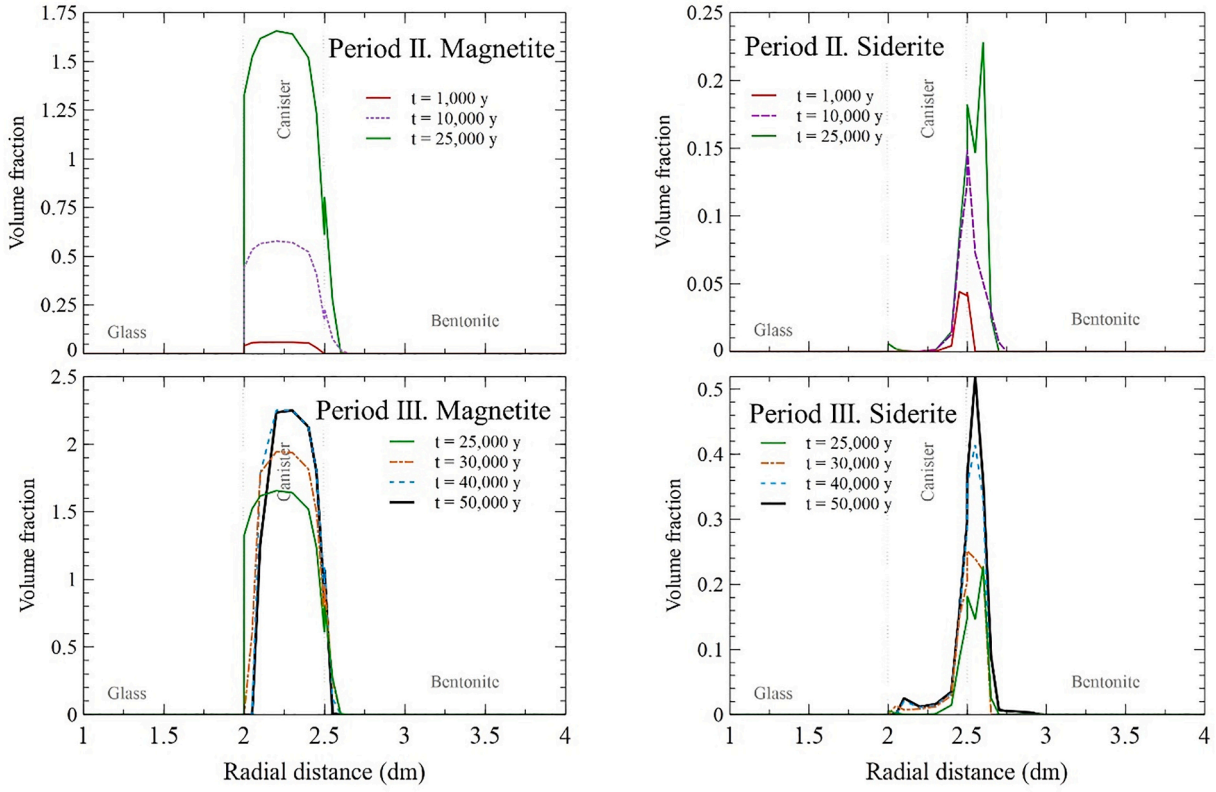

Fig. 3. Spatial distribution of the computed volume fraction of magnetite (left) and siderite (right) at selected times of Periods II (top) and III (bottom).

magnetite precipitation band in the bentonite was about 1 cm at t = 25,000 years. Siderite precipitated at both sides of the canister/bentonite interface (Fig. 3). The precipitation front penetrated in the bentonite about 1 cm. Goethite did not precipitate.

The greenalite volume fraction increased with time in the canister, especially near the bentonite interface and in the bentonite. The thickness of the greenalite precipitation band in the bentonite was larger than those of magnetite and siderite. Greenalite was the main corrosion product in the bentonite (Fig. 4). Smectite dissolution increased with time and was largest near the canister interface (Fig. 4). Smectite dissolution triggered the precipitation of a small amount of Mg-saponite in the bentonite at t = 25,000 years (not shown here). Mg-nontronite did not precipitate. Calcite precipitated in the canister near the bentonite interface, in the bentonite and in the granite (Fig. 3 in the SM). Gypsum did not precipitate.

The concentration of Cl^- decreased with time in the bentonite due solute diffusion from the bentonite into the granite because the initial Cl^- concentration in the granite porewater ($3.95{\cdot}10^{-4}$ M) is much smaller than the initial concentration in the bentonite ($2.75{\cdot}10^{-1}$ M) (Fig. 4 in SM). The profiles of the concentration of Cl^- showed very small gradients because the solute transfer from the bentonite into the granite is not controlled by solute diffusion through the bentonite, but by solute advection and diffusion in the granite. The computed concentrations of dissolved Ca^{2+}, Mg^{2+}, Na^+ and K^+ decreased with time due to solute diffusion into the granite (not shown here). On the other hand, the computed concentration of dissolved aluminum in the bentonite increased with time due to smectite dissolution (Fig. 5 in SM). Glass dissolution was disabled in Period II until canister failure.

The concentrations of exchanged Ca^{2+} and Mg^{2+} were the largest with values around 43 and 37 meq/100 g, respectively (Fig. 6 in SM). The concentration of exchanged Na^+ was 22 meq/100 g while that of potassium was equal to 1.6 meq/100 g. The concentration of exchanged Fe^{2+} was largest near the canister interface and decreased with distance from the canister interface. The spatial distribution of the concentration of exchanged Fe^{2+} is like that of the concentration of dissolved Fe^{2+}. The concentration of S^sOFe^+ was the largest in the strong sorption sites (Fig. 7 in SM). The concentration of S^sOFeOH in the strong sorption sites showed a clear peak near the canister interface. The concentration of $S^{w1}O^-$ in the weak #1 sorption sites was largest near the canister interface and decreased with distance from such interface while the concentration of $S^{w1}OH$ increased. The concentration of $S^{w1}OFe^+$ in weak #1 sorption sites showed also a maximum near the canister interface. The concentrations of the surface complexes in weak #2 sites showed small changes because Fe was not sorbed on these sites.

6. Model results for Period III

Period III started after canister failure at 25,000 years and considered glass dissolution and the interactions of glass with corrosion products and uncorroded carbon steel. The final time of simulation of this period was 50,000 years.

Computed ISG dissolution increased with time from t = 25,000 to t = 50,000 years. Model results showed a dissolution front which moves into the glass (Fig. 5). Glass dissolution led to an increase of pH with time in the glass (Fig. 2). The concentration of dissolved silica increased in the inner part of the glass until t = 30,000 years (Fig. 8 in SM). The concentration of dissolved silica in the outer part of the glass decreased with time due to the diffusion of dissolved silica from the glass into the canister and the bentonite. This diffusive flux caused the precipitation of greenalite at the glass/canister and canister/bentonite interfaces. The pH at t = 50,000 years ranged from 7.93 to 7.89 in the glass, from 7.89 to 8.66 in the canister and from 7.87 to 8.6 in the bentonite.

Magnetite precipitated in the canister after 25,000 years while the remaining carbon steel corroded. Once the canister was fully corroded, magnetite redissolved near the glass/canister interface and greenalite precipitated (Figs. 3 and 4). Greenalite precipitated in the canister and the bentonite, especially at the glass/canister interface. Siderite precipitated at the canister/bentonite interface (Fig. 3). Goethite did not

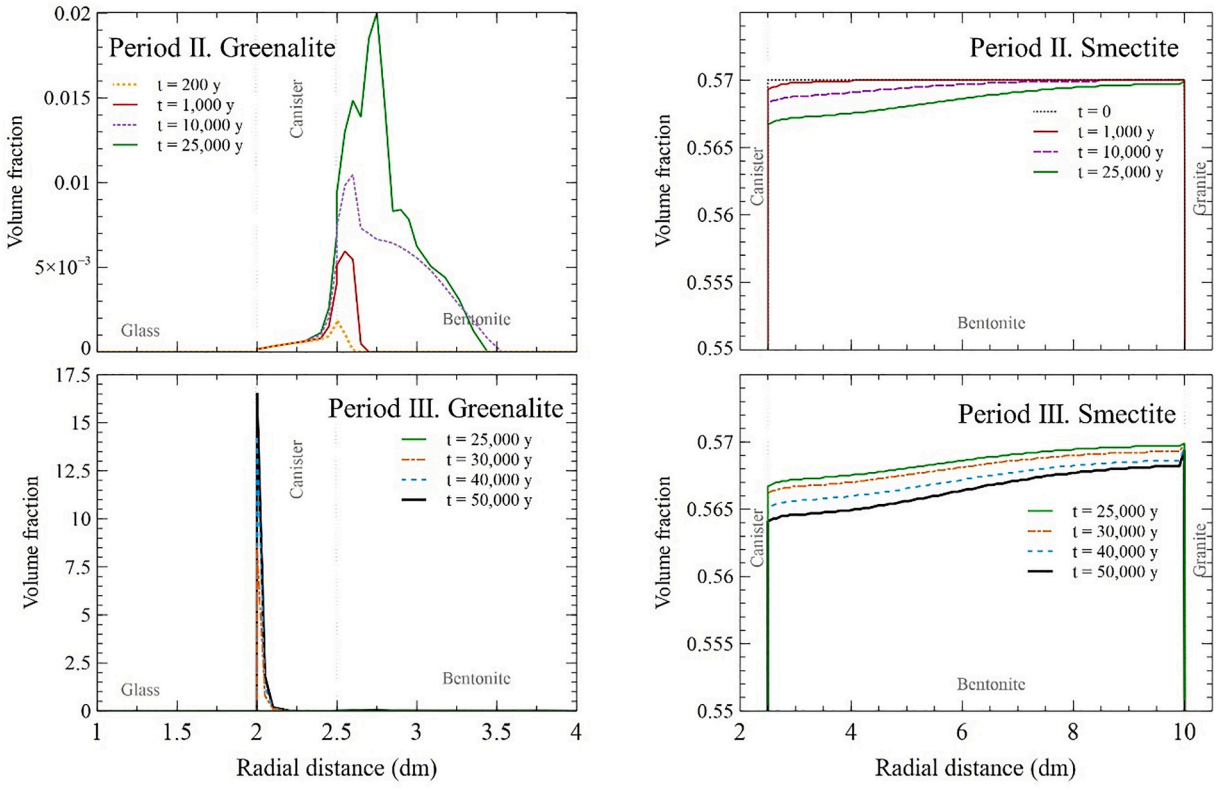

Fig. 4. Spatial distribution of the computed volume fractions of greenalite (left) and smectite (right) at selected times of Periods II (top) and III (bottom).

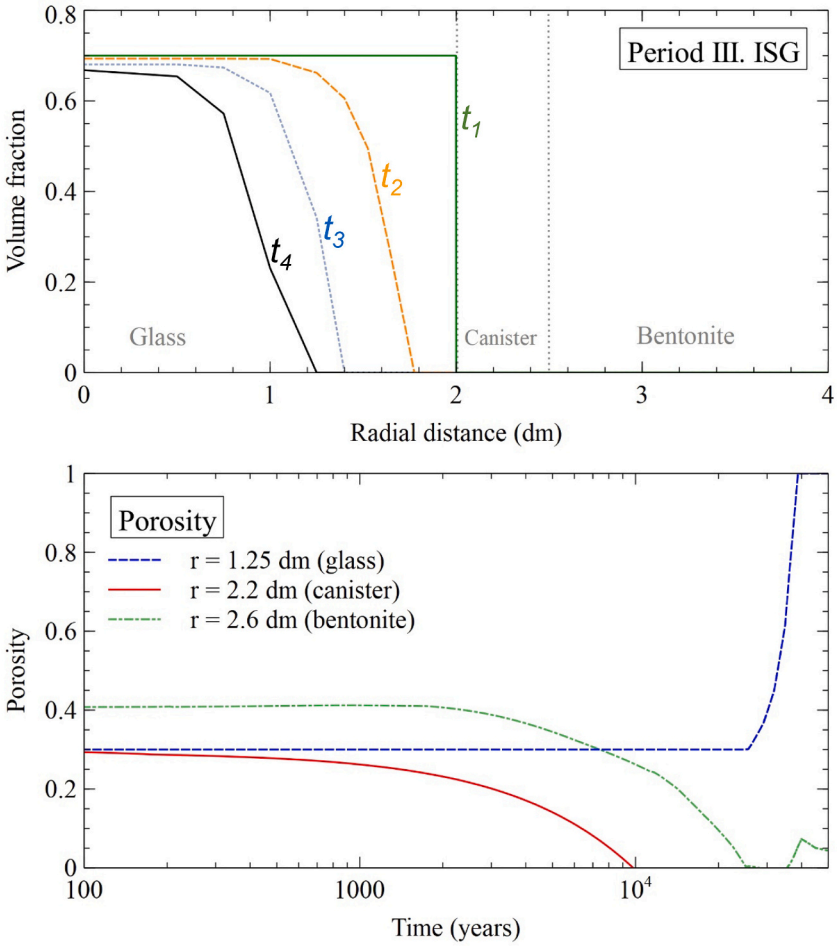

Fig. 5. Spatial distribution of the computed volume fraction of ISG at selected times (t_1 = 25,000, t_2= 30,000, t_3 = 40,000 and t_4 = 50,000 years) of Period III (top) and time evolution of the porosity changes caused by mineral dissolution/precipitation during Periods II and III in the glass (r = 12.5 cm), the canister (r = 22 cm) and the bentonite (r = 26.5 cm) (bottom).

precipitate.

Smectite dissolution kept increasing with time from t = 25,000 to t = 50,000 years and was largest near the canister interface (Fig. 4). Smectite dissolution triggered Mg-saponite precipitation in the bentonite (in a small amount) and especially in the canister near the glass/canister interface (Fig. 9 in SM). Mg-nontronite did not precipitate. Calcite re-dissolved in the canister and in the bentonite/canister interface at 50,000 years (Fig. 10 in SM).

Porosity in the glass zone did not change in Period II ($t \leq$ 25,000 years) because glass dissolution was disabled (Fig. 5). The porosity of the glass increased after 25,000 years due to glass dissolution and the modeling simplification that the precipitation of secondary solid phases (as silica gel) was prevented in the glass. The calculated porosity in the canister decreased due to calcite, magnetite, siderite and greenalite precipitation. Pore clogging was predicted to occur in this location at t = 10,000 years. The porosity in the bentonite at 1 cm from the canister interface decreased with time due to the precipitation of calcite, siderite and greenalite, kept decreasing until t = 28,000 years, when reached clogging due to the precipitation of siderite and calcite and later increases slightly up to 0.05.

The concentration of dissolved Cl^- at the canister, the bentonite and the granite kept decreasing from t = 25,000 to t = 50,000 years, reaching a uniform concentration equal to $6.9{\cdot}10^{-4}$ M in the three materials at t = 50,000 years (Fig. 11 in SM). The trends of the computed concentrations of dissolved Al^{3+}, Ca^{2+}, Mg^{2+}, Na^+ and K^+ were similar. The concentrations increased from t = 25,000 to t = 30,000 years and later decreased (not shown here).

The concentration of dissolved Fe^{2+} in the glass decreased from t = 25,000 to t = 50,000 years (Fig. 2). The concentration of dissolved Fe^{2+} in the canister, however, increased due to the re-dissolution of magnetite. The concentration was largest near the glass interface. The peak of the concentration of dissolved Fe moved slightly towards the canister/bentonite interface.

The concentrations of exchanged Ca^{2+}, Mg^{2+}, $Na^+$and K^+ in the bentonite were uniform (Fig. 12 in SM). The concentration of exchanged Na in Period III increased from 22 to 26 meq/100 g while that of exchanged Ca^{2+}increased from 43 to 55 meq/100 g. The concentration of exchanged Mg^{2+}, however, decreased from 37 to 18 meq/100 g. The concentration of exchanged K^+ showed no major changes. The concentration of exchanged Fe^{2+} at t = 50,000 years decreased with distance from the canister interface in a manner like Period II. The peaks of the concentrations of S^sOFe^+ and S^sOFeOH in strong sites and $S^{w1}OFe^+$ in weak #1 sites near the canister interface were similar to those computed at t = 25,000 years (Fig. 13 in SM).

The thickness of the bentonite enriched in Fe increased with time. The fronts of sorbed and dissolved Fe^{2+} penetrated 0.035 m into bentonite at t = 25,000 years and 0.174 m at t = 50,000 years. The front of exchanged iron penetrated 0.03 m and 0.156 m into the bentonite at 25,000 and 50,000 years, respectively. The thickness of the bentonite affected by corrosion products increased from 0.104 m at 25, 000 years to 0.174 m at 50,000 years (see Fig. 14 and Table 4 in SM).

7. Sensitivity cases

Model sensitivity runs were performed to: 1) Evaluate model uncertainties caused by uncertainties in model parameters; 2) Consider other model hypotheses, and 3) Evaluate the relevance of model simplifications. The following sensitivity cases were carried out: 1) A decrease of the threshold silica concentration in the kinetic glass dissolution rate; 2) An increase in the groundwater water flux in the granite; 3) A porosity feedback effect; 4) A variable corrosion rate depending on temperature and Fe(0) saturation index; 5) A reduction of the time for canister failure from $t = 25{,}000$ years to $t = 10{,}000$ years, and 6) A model without smectite dissolution.

The results of the sensitivity cases indicated that (Fig. 15 in SM): 1) Model predictions were sensitive to a decrease of C_{Si}* from 10^{-3} to $5{\cdot}10^{-4}$ mol/L. A decrease in C_{Si}* led to a decrease in glass dissolution rate; 2) The larger, the granite flux the larger the decrease of solute concentrations in the bentonite. The precipitation of corrosion products was slightly sensitive to the increase in granite flux (Figs. 16 and 17 in SM); 3) Model results were very sensitive to the porosity feedback effect (PFE) because the porosity reaches the threshold value in the canister. Pore clogging prevents further precipitation and decreases solute diffusion coefficient. Magnetite precipitation stopped when the threshold porosity was reached. Glass dissolution reduced drastically when the PFE was considered because the dissolution rate depends on pH and silica concentration. The glass dissolution rate dropped to the residual dissolution rate; 4) The corrosion rate and the precipitation of corrosion products were much smaller than those of the base run when the corrosion rate was assumed to depend on temperature and Fe(0) saturation index. Glass dissolution was not affected by the consideration of a variable corrosion rate; 5) Model results were not very sensitive to smectite dissolution, and 6) Shortening the duration of Period II from $t = 25{,}000$ years to $t = 10{,}000$ years had a significant impact in the glass dissolution front at $t = 50{,}000$ years and led to a decrease of the precipitation of corrosion products because greenalite precipitated instead of magnetite and siderite.

8. Conclusions

A reactive transport model of the geochemical evolution of a HLW disposal cell in granite has been presented. The model considers Periods II (canister corrosion) and III (glass dissolution).

The concentrations of most dissolved species in the bentonite in Period II decrease with time due to out diffusion from the bentonite into the granite because the initial concentrations in the granite porewater are much smaller than the initial concentrations in the bentonite. Canister corrosion causes an increase in pH. The computed pH at the end of Period II (25,000 years) is 9.25 in the canister and ranges from 9.25 to 7.82 in the bentonite. The corrosion products predicted in Period II include magnetite, siderite and greenalite. The thickness of magnetite precipitation band in the bentonite at $t = 25{,}000$ years is about 1 cm. Siderite precipitates at both sides of the canister/bentonite interface. The precipitation front penetrates >1 cm into the bentonite. Greenalite is the main corrosion product in the bentonite in Period II. Smectite dissolution triggers the precipitation of a small amount of Mg-saponite in the bentonite. Calcite precipitates in the canister near the bentonite/canister interface, the bentonite and the granite.

Period III starts after canister failure at $t = 25{,}000$ years. Glass dissolution leads to an increase of pH. The diffusive flux of dissolved silica causes the precipitation of greenalite at the glass/canister and canister/bentonite interfaces. The pH at $t = 50{,}000$ years ranges from 7.93 to 7.89 in the glass, from 7.89 to 8.66 in the canister and from 7.87 to 8.6 in the bentonite. Magnetite precipitates in the canister while there is carbon steel to corrode. Once the canister is fully corroded, magnetite re-dissolves near the glass/canister interface and greenalite precipitates. Greenalite precipitates in the canister and the bentonite, especially at the glass/canister interface. Siderite precipitates at the canister/bentonite interface and goethite does not precipitate. Calcite re-dissolves in the canister and the bentonite/canister interface at $t = 50{,}000$ years. The porosity in the glass increases due to glass dissolution.

The porosity in the canister decreases and pore clogging is predicted at $t = 10{,}000$ years due to calcite, magnetite, siderite and greenalite precipitation. The porosity in the bentonite at 1 cm from the canister interface continues to decrease from $t = 25.000$ to $t = 28{,}000$ years, when reaches clogging due to the precipitation of siderite and calcite. After 35,000 years, the porosity increases slightly and remains smaller than 0.05 at $t = 50{,}000$ years.

The reactive transport model of the geochemical evolution of a HLW disposal cell in granite presented here has limitations and uncertainties. The model could be expanded and improved by: 1) Considering a 2D axisymmetric model; 2) Replacing the assumption of porous canister by a model of progressive canister corrosion with a dynamic update of material properties; 3) Considering the initial aerobic corrosion stage (Period I), the consumption of oxygen and the precipitation of Fe(III) oxides, hydroxides and oxyhydroxides (Mon et al., 2023); 4) Adopting a more realistic complex glass dissolution model such as the GRAAL model (Frugier et al., 2008, 2018); 5) Including radioactive elements in the vitrified waste chemical composition; 6) Adopting a multiple porosity model with adsorbed, interlayer and free water; and 7) Using different diffusion coefficients for each dissolved species.

CRediT authorship contribution statement

Luis Montenegro: Conceptualization, Software, Validation, Writing – original draft. **Javier Samper:** Conceptualization, Investigation, Validation, Supervision, Writing – review & editing. **Alba Mon:** Methodology, Software, Visualization, Writing – original draft. **Laurent De Windt:** Validation, Writing – review & editing. **Aurora-Core Samper:** Visualization, Software. **Enrique García:** Funding acquisition, Supervision.

Declaration of Competing Interest

The authors declare that they have no known competing financial interests or personal relationships that could have appeared to influence the work reported in this paper.

Data availability

Data will be made available on request.

Acknowledgements

The research leading to these results was funded by ENRESA within the Work Package ACED of EURAD (European Joint Programme on Radioactive Waste Management of the European Union, EC grant agreement nº 847593), the Spanish Ministry of Science and Innovation (PID2019-109544RB-I00) and the Galician Regional Government (Grant ED431C2021/54). Funding for open access charge was provided by Universidade da Coruña/CISUG. We thank Diederik Jacques, leader of the ACED Work Package, and the ACED members for many enriching discussions, suggestions and recommendations, Erika Neeft (COVRA) for providing the temperature curves, and the special editor and the two anonymous reviewers for their comments and corrections.

Appendix A. Supplementary data

Supplementary data to this article can be found online at https://doi.org/10.1016/j.clay.2023.107018.

References

Águila, J.F., Samper, J., Mon, A., Montenegro, L., 2020. Dynamic update of flow and transport parameters in reactive transport simulations of radioactive waste repositories. Appl. Geochem. 117, 104585 https://doi.org/10.1016/j.apgeochem.2020.104585.

Águila, J.F., Montoya, V., Samper, J., Kosakowski, G., Krejci, P., Pfingsten, W., Montenegro, Luis, 2021. Modelling Cs migration through Opalinus clay: a benchmark for single- and multi-species sorption-diffusion models. Comput. Geosci. https://doi.org/10.1007/s10596–021–10050-5.

Appelo, C.A.J., Postma, D., 1993. Geochemistry, Groundwater and Pollution. A.A. Balkema, Brookfield, Vt.

Bildstein, O., Claret, F., 2015. Chapter 5-Stability of Clay Barriers under Chemical Perturbations. In: Tournassat, C., Steefel, C.I., Bourg, I.C., Faiza, B. (Eds.), Developments in Clay Science, Vol. 6. Elsevier, pp. 155–188.

Bildstein, O., Trotignon, L., Perronnet, M., Jullien, M., 2006. Modelling iron-clay interactions in deep geological disposal conditions. Phys. Chem. Earth Parts A/B/C 31, 618–625.

Bildstein, O., Trotignon, L., Pozo, C., Jullien, M., 2007. Modelling glass alteration in an altered argillaceous environment. J. Nucl. Mater. 362, 493–501.

Bildstein, O., Lartigue, J., Pointeau, I., Cochepin, B., Munier, I., Michau, N., 2012. Chemical evolution in the near field of HLW cells: Interactions between glass, steel and clay-stone in deep geological conditions. In: 5th ANDRA International Meeting, 22–25 Oct 2012, Montpellier, France.

Bildstein, O., Claret, F., Frugier, P., 2019. RTM for waste repositories. Rev. Mineral. Geochem. 85, 419–457.

Bradbury, M.H., Baeyens, B., 1997. A mechanistic description of Ni and Zn sorption on Na-montmorillonite. Part II: modelling. J. Contam. Hydrol. 27, 223–248.

Bradbury, M.H., Baeyens, B., 2005. Modelling the sorption of Mn(II), Co(II), Ni(II), Zn (II), Cd(II), Eu(III), Am(III), Sn(IV), Th(IV), Np(V) and U(VI) on montmorillonite: linear free energy relationships and estimates of surface binding constants for some selected heavy metals and actinides. Geochim. Cosmochim. Acta 69, 875–892.

Cama, J., Ganor, J., Ayora, C., Lasaga, C.A., 2000. Smectite dissolution kinetics at 80°C and pH 8.8. Geochim. Cosmochim. Acta 64, 15, 2701–2717.

Chaparro, M.C., Finck, N., Metz, V., Geckeis, H., 2021. Reactive transport modelling of the long-term interaction between carbon steel and MX-80 bentonite at 25°C. Minerals 11, 1272. https://doi.org/10.3390/min11111272.

Claret, F., Marty, N., Tournassat, C., 2018. Modeling the long-term stability of multibarrier systems for nuclear waste disposal in geological clay formations. In: Xiao, Y., Whitaker, F., Xu, T., Steefel, C. (Eds.), Reactive Transport Modeling: Applications in Subsurface Energy and Environmental Problems. Wiley, pp. 395–436.

Claret, F., Dauzeres, A., Jacques, D., Sellin, P., Cochepin, B., De Windt, L., Garibay-Rodriguez, J., Govaerts, J., Leupin, O., Mon Lopez, A., Montenegro, L., Montoya, V., Prasianakis, N.I., Samper, J., Talandier, J., 2022. Modelling of the long-term evolution and performance of engineered barrier system. EPJ Nuc. Sci. Technol. 8, 41.

De Windt, L., Spycher, N.F., 2019. Reactive transport modeling: a key performance assessment tool for the geologic disposal of nuclear waste, elements: Int. Mag. Mineral. Geochem. Petrol. 15, 99.

De Windt, L., Leclercq, S., van der Lee, J., 2006. Assessing the durability of nuclear glass with respect to silica controlling processes in a clayey underground disposal. Mater. Res. Soc. Proc. 932, 313–320.

Debure, M., Frugier, P., De Windt, L., Gin, S., 2012. Borosilicate glass alteration driven by magnesium carbonates. J. Nucl. Mater. 420, 347–361.

Debure, M., De Windt, L., Frugier, P., Gin, S., 2013. HLW glass dissolution in the presence of magnesium carbonate: Diffusion cell experiment and coupled modeling of diffusion and geochemical interactions. J. Nucl. Mater. 443, 507–521.

Debure, M., Linard, Y., Martin, C., Claret, F., 2019. In situ nuclear-glass corrosion under geological repository conditions. Mater. Degrad. 3, 38.

Deissmann, G., Ait, Mouheb N., Martin, C., Turrero, M.J., Torres, E., Kursten, B., Weetjens, E., Jacques, D., Cuevas, J., Samper, J., Montenegro, L., Leivo, M., Somervuori, M., Carpen, L., 2021. Experiments and numerical model studies on interfaces. Final version as of 11.05.2021 of deliverable D2.5 of the HORIZON 2020 project EURAD. EC Grant agreement no: 847593.

ENRESA, 2001. ENRESA 2000. Evaluación del comportamiento y de la seguridad de un almacén geológico profundo de residuos radiactivos en arcilla. ENRESA (in Spanish).

ENRESA, 2006. FEBEX: Updated final report 1994-2004. ENRESA Technical Publication PT 05-0/2006.

Fernández, J., 2017. Reactive Transport Models of Low Permeability Structured Porous and Fractured Media. Ph.D. Dissertation. Universidad de A Coruña, Spain.

Fernández, A.M., Baeyens, B., Bradbury, M., Rivas, P., 2004. Analysis of the pore water chemical composition of a Spanish compacted bentonite used in an engineered barrier. Phys. Chem. Earth 29 (1), 105–118.

Fernández, R., Cuevas, J., Mäder, U., 2009. Modelling concrete interaction with a bentonite barrier. Eur. J. Mineral. 21, 177–191.

Fleury, B., Godon, N., Ayral, A., Perret, D., Dussossoy, J.-L., Gin, S., 2014. Development of an experimental design to investigate the effects of R7T7 glass composition on the residual rate of alteration. Procedia Mater. Sci. 7, 193–201.

Frugier, P., Gin, S., Minet, Y., Chave, T., Bonin, B., Godon, N., Lartigue, J.E., Jollivet, P., Ayral, A., De Windt, L., Santarini, G., 2008. SON68 nuclear glass dissolution kinetics: current state of knowledge and basis of the new GRAAL model. J. Nucl. Mater. 380, 8–21.

Frugier, P., Rajmohan, N., Minet, Y., Godon, N., Gin, S., 2018. Modeling glass corrosion with GRAAL. Mater. Degrad. 2, 35.

Giffaut, E., Grivé, M., Blanc, P., Vieillard, P., Colàs, E., Gailhanou, H., Gaboreau, S., Marty, N., Madé, B., Duro, L., 2014. Andra thermodynamic database for performance assessment: ThermoChimie. Appl. Geochem. 49, 225–236.

Gin, S., Frugier, P., 2002. SON68 glass dissolution kinetics at high reaction progress: experimental evidence of the residual rate. MRS Online Proc. Lib. (OPL) 757.

Gin, S., Abdelouas, A., Criscenti, L.J., Ebert, W.L., Ferrand, K., Geisler, T., Harrison, M.T., Inagaki, Y., Mitsui, S., Mueller, K.T., Marra, J.C., Pantano, C.G., Pierce, E.M., Ryan, J.V., Schofield, J.M., Steefel, C.I., Vienna, J.D., 2013. An international initiative on long-term behaviour of high-level nuclear waste glass. Mater. Today 16, 243–248.

Gin, S., Jollivet, P., Fournier, M., Berthon, C., Wang, Z., Mitroshkov, A., Zhu, Z., Ryan, J. V., 2015. The fate of silicon during glass corrosion under alkaline conditions: a mechanistic and kinetic study with the International Simple Glass. Geochim. Cosmochim. Acta 15, 68–85.

Jollivet, P., Minet, Y., Nicolas, M., Vernaz, É., 2000. Simulated alteration tests on non-radioactive SON 68 nuclear glass in the presence of corrosion products and environmental materials. J. Nucl. Mater. 281, 231–243.

Jollivet, P., Gin, S., Schumacher, S., 2012. Forward dissolution rate of silicate glasses of nuclear interest in clay-equilibrated groundwater. Chem. Geol. 330–331, 207–217.

Lu, C., Samper, J., Fritz, B., Clement, A., Montenegro, L., 2011. Interactions of corrosion products and bentonite: an extended multicomponent reactive transport model. Phys. Chem. Earth 36, 1661–1668. https://doi.org/10.1016/j.pce.2011.07.013.

Marty, N.C.M., Fritz, B., Clement, A., Michau, N., 2010. Modelling the long-term alteration of the engineered bentonite barrier in an underground radioactive waste repository. Appl. Clay Sci. 47, 82–90.

Molinero, J.J., Samper, G. Zhang, Yang, C., 2004. Biogeochemical reactive transport model of the redox zone experiment of the Äspö hard rock laboratory in Sweden. Nucl. Technol. 148, 151–165.

Mon, A., Samper, J., Montenegro, L., Naves, A., Fernández, J., 2017. Reactive transport model of compacted bentonite, concrete and corrosion products in a HLW repository in clay. J. Contam. Hydrol. 197, 1–16.

Mon, A., Samper, J., Montenegro, L., Turrero, M.J., Torres, E., Cuevas, J., Fernández, R., De Windt, L., 2023. Reactive transport models of the geochemical interactions at the iron/bentonite interface in laboratory corrosion tests. Appl. Clay Sci. https://doi.org/10.1016/j.clay.2023.106981 (this issue).

Neeft, E., Weetjens, E., Vokal, A., Leivo, M., Cochepin, B., Martin, C., Munier, I., Deissmann, G., Montoya, V., Poskas, P., Grigaliuniene, D., Narkuniene, A., García, E., Samper, J., Montenegro, L., Mon, A., 2020. Treatment of chemical evolution in National Programmes, Deliverable 2.4 of the HORIZON 2020 project EURAD. EC Grant agreement no: 847593.

Ortiz, L., Volckaert, G., Mallants, D., 2002. Gas generation and migration in Boom clay, a potential host rock formation for nuclear waste storage. Eng. Geol. 64, 287–296.

Poonoosamy, J., Wanner, C., Alt Epping, P., Águila, J., Samper, J., Montenegro, L., Xie, M., Su, D., Mayer, U., Mäder, U., Van Loon, L.R., Kosakowski, G., 2018. Benchmarking of reactive transport codes for a 2D setup with mineral dissolution/precipitation reactions and feedback on transport parameters. Comput. Geosci. https://doi.org/10.1007/s10596-018-9793-x.

Samper, J., Dai, Z., Molinero, J., García-Gutiérrez, M., Missana, T., Mingarro, M., 2006. Inverse modeling of tracer experiments in FEBEX compacted Ca-bentonite. Phys. Chem. Earth 31, 640–648.

Samper, J., Lu, C., Montenegro, L., 2008. Coupled hydrogeochemical calculations of the interactions of corrosion products and bentonite. Phys. Chem. Earth 33, S306–S316. https://doi.org/10.1016/j.pce.2008.10.009.

Samper, J., Xu, T., Yang, C., 2009. A sequential partly iterative approach for multicomponent reactive transport CORE^{2D}. Comput. Geosci. 13, 301–316.

Samper, J., Naves, A., Montenegro, L., Mon, A., 2016. Reactive transport modelling of the long-term interactions of corrosion products and compacted bentonite in a HLW repository in granite: uncertainties and relevance for performance assessment. Appl. Geochem. 67, 42–51.

Samper, J., Mon, A., Montenegro, L., 2018. A revisited thermal, hydrodynamic, chemical and mechanical model of compacted bentonite for the entire duration of the FEBEX in situ test. Appl. Clay Sci. 160, 58–70. https://doi.org/10.1016/j.clay.2018.02.019.

Samper, J., Montenegro, L., De Windt, L., Montoya, V., Garibay-Rodríguez, J., Grigaliuniene, D., Narkuniene, A., Poskas, P., 2022. Conceptual model formulation for a mechanistic based model implementing the initial SOTA knowledge (models and parameters) in existing numerical tools. In: Deliverable D2.16 of the EURAD Joint Project. EC Grant Agreement no: 847593.

Savage, D., 2012. Prospects for Coupled Modelling. Report STUK-TR 13, STUK, Helsinki, Finland.

Savage, D., Watson, C., Benbow, S., Wilson, J., 2010. Modelling iron-bentonite interactions. Appl. Clay Sci. 47, 91–98.

Tournassat, C., Lerouge, C., Blanc, P., Brendlé, J., Greneche, J.M., Touzelet, S., Gaucher, E.C., 2008. Cation exchanged Fe(II) and Sr compared to other divalent cations (Ca, Mg) in the Bure Callovian–Oxfordian formation: implications for porewater composition modelling. Appl. Geochem. 23 (4), 641–654.

Xu, T., Senger, R., Finsterle, S., 2008. Corrosion-induced gas generation in a nuclear waste repository: reactive geochemistry and multiphase flow effects. Appl. Geochem. 23, 3423–3433.

Zhang, G., Samper, J., Montenegro, L., 2008. Coupled thermo-hydro-bio-geochemical reactive transport model of the CERBERUS heating and radiation experiment in

Boom clay. Appl. Geochem. 23 (4), 932–949. https://doi.org/10.1016/j.apgeochem.2007.09.010.
Zheng, L., Samper, J., 2008. A coupled THMC model of FEBEX mock-up test. Phys. Chem. Earth 33, S486–S498.
Zheng, L., Samper, J., Montenegro, L., 2011. A coupled THC model of the FEBEX in situ test with bentonite swelling and chemical and thermal osmosis. J. Contam. Hydrol. 126, 45–60.